



## *CloudSat* Precipitation Profiling Algorithm—Model Description

CRISTIAN MITRESCU

*Naval Research Laboratory, Monterey, California*

TRISTAN L'ECUYER

*Colorado State University, Fort Collins, Colorado*

JOHN HAYNES

*Monash University, Clayton, Australia*

STEVEN MILLER

*Cooperative Institute for Research in the Atmosphere, Fort Collins, Colorado*

JOSEPH TURK

*Jet Propulsion Laboratory, Pasadena, California*

(Manuscript received 7 January 2009, in final form 17 December 2009)

### ABSTRACT

Identifying and quantifying the intensity of light precipitation at global scales is still a difficult problem for most of the remote sensing algorithms in use today. The variety of techniques and algorithms employed for such a task yields a rather wide spectrum of possible values for a given precipitation event, further hampering the understanding of cloud processes within the climate. The ability of *CloudSat's* millimeter-wavelength Cloud Profiling Radar (CPR) to profile not only cloud particles but also light precipitation brings some hope to the above problems. Introduced as version zero, the present work uses basic concepts of detection and retrieval of light precipitation using spaceborne radars. Based on physical principles of remote sensing, the radar model relies on the description of clouds and rain particles in terms of a drop size distribution function. Use of a numerical model temperature and humidity profile ensures the coexistence of mixed phases otherwise undetected by the CPR. It also provides grounds for evaluating atmospheric attenuation, important at this frequency. Related to the total attenuation, the surface response is used as an additional constraint in the retrieval algorithm. Practical application of the profiling algorithm includes a 1-yr preliminary analysis of global rainfall incidence and intensity. These results underscore once more the role of *CloudSat* rainfall products for improving and enhancing current estimates of global light rainfall, mostly at higher latitudes, with the goal of understanding its role in the global energy and water cycle.

### 1. Introduction

Clouds play an important role in the climate system through complex, nonlinear feedback processes involving radiation, chemistry, atmospheric dynamics and thermodynamics, and surface–atmospheric coupling (Held and

Soden 2000). As an integral component of the earth's hydrological cycle, clouds are essential in sustaining many forms of life on land through delivery of freshwater to the surface and subsurface storage aquifers in the form of precipitation. Given the widely varying spatial and temporal distribution of precipitating cloud systems, satellite remote sensing is the most practical option for monitoring the global distribution and intensity of this quantity. Moreover, given the three-dimensional structure of precipitation, active observing systems such as radars represent the best suited instruments for this purpose.

---

*Corresponding author address:* Cristian Mitrescu, Science Systems and Applications, Inc., One Enterprise Pkwy., Suite 200, Hampton, VA 23666.  
E-mail: cristian.mitrescu@ssaihq.com

The primary objective of *CloudSat*, a National Aeronautics and Space Administration (NASA) Earth System Science Pathfinder satellite mission launched on 28 April 2006, is to provide, from space, the first global survey of cloud vertical structure, layering, and content. Placed in a sun-synchronous polar orbit (1330 local time ascending node), *CloudSat* is capable of capturing the seasonal and geographical distributions necessary to evaluate, understand, and ultimately improve the way clouds and cloud feedbacks are handled within global weather and climate forecast models (Stephens et al. 2002). With its nominal 2-yr mission lifetime having been extended in for an additional 3.5 yr (contingent on the health of the spacecraft and sensor), the value of *CloudSat* measurements to climate research continues to increase.

The “A-Train” constellation of satellites, of which *CloudSat* is a member, is aimed at studying a full suite of surface and atmospheric characteristics using an impressive array of sensors, both active and passive that encompass a wide spectral range of frequencies. *CloudSat* follows immediately behind the NASA *Aqua* satellite in the A-Train. *Aqua* carries a suite of passive sensors such as the Atmospheric Infrared Sounder/Advanced Microwave Sounding Unit (AIRS/AMSU), Advanced Microwave Scanning Radiometer for Earth Observing System (AMSR-E), Clouds and the Earth’s Radiant Energy System (CERES), and Moderate Resolution Imaging Spectroradiometer (MODIS; <http://aqua.nasa.gov>). The Cloud–Aerosol Lidar and Infrared Pathfinder Satellite Observations (CALIPSO) satellite, carrying the Cloud–Aerosol Lidar with Orthogonal Polarization (CALIOP) lidar, trails closely behind *CloudSat* in tight formation to achieve maximum overlap between the observations. CALIOP is most sensitive to thin high-level cirrus, aerosols, and boundary layer structures, providing a complementary observation to *CloudSat*. Polarization and Anisotropy of Reflectances for Atmospheric Sciences coupled with Observations from a Lidar (PARASOL) and *Aura* round off the A-Train formation.

This paper provides an update on progress to exploit the sensitivity of *CloudSat* to light rainfall. Described herein is an algorithm and methodology for quantifying profiles of rain rate from measurements of radar backscatter. The technique is designed to augment the existing suite of level-2 environmental data records produced by *CloudSat*. In light of the multiple challenges (both algorithmic and sensor hardware) associated with harnessing the potential of this new sensor dataset, the results presented here are regarded as preliminary.

## 2. *CloudSat*’s 94-GHz observing system

*CloudSat* carries the Cloud Profiling Radar, a 94-GHz nadir-pointing radar that has a sensitivity of around

–28 dB, an 80-dB dynamic range, 240-m vertical resolution (oversampled from a 480-m pulse length), and a 1.7 km × 1.3 km footprint. It samples 688 pulses to form a single profile, with spacecraft motion over that interval resulting in 1.1-km horizontal resolution. Unlike ground-based radars that use centimeter wavelengths, *CloudSat*’s millimeter operating wavelength (3 mm) provides sensitivity to lighter precipitation (missed by conventional terrestrial weather radar systems) and even the smaller ice and/or liquid particles composing the cloud itself. From its satellite vantage point, the Cloud Profiling Radar (CPR) beam is unobstructed by elevated terrain, in contrast to ground-based radars. Although *CloudSat* provides global coverage, its nadir-only viewing geometry (nonscanning) results in “curtain” observations (2D slices through the atmosphere) as opposed to the 3D volume capability of a scanning sensor. Mitigating this limitation are passive scanning sensors on the A-Train that offer a wider 2D view of the scene within seconds–minutes of the CPR observation. Moreover, the suite of all other geostationary satellites offers the much needed spatial and temporal continuum that complements the polar-orbiting A-Train system. It follows that a combination of such sensors can provide a nearly 3D scan of the atmosphere. Combinations of these sensors are already being used to characterize the global distribution of clouds (Mace et al. 2009) and to study the impact of aerosols on cloud optical and microphysical properties (Lebsock et al. 2008). A near-real-time application of CPR scans and associated products are already being applied (Mitrescu et al. 2008).

## 3. *CloudSat* light precipitation profiling algorithm

The CPR on board *CloudSat* measures backscatter reflectivity as a function of distance from both distributed (i.e., hydrometeors) and solid (i.e., surface) targets. The physical basis for the profiling algorithm resides in the physical relationship between the return power, measured as a function of distance to the target, and the cloud, precipitation, and surface properties. Given that its frequency of operation (94 GHz) resides in a “dirty window” of the atmosphere where water vapor is slightly absorptive, the measured signal is subject to both cloud and atmospheric attenuation, which must be taken into account. Because of the large volume sampled by the CPR, the returned power at a given range often is increased because of multiply-scattered photons. A component of this multiply-scattered energy leads to a loss of correct ranging capability, since the signal may have come from other regions of the cloud. These effects increase with the penetration depth and with the size of cloud particles. As such, the ability to accurately simulate CPR observations (and thereby retrieve physical

TABLE 1. Rainfall retrieval microphysical parameters.

Parameter	$a$ (m)	$b$	$N_0$ (m <sup>6</sup> )
Snow	4100	0.21	$8.0 \times 10^{-18}$
Rain	1756	0.27	$8.0 \times 10^{-18}$

parameters) becomes increasingly more challenging for range gates closer to the ground (i.e., farther away from radar), which is where the precipitation occurs. The following subsections describe the procedures followed to account for the various physical mechanisms influencing the CPR measurements.

#### a. Cloud microphysical model

The purpose of developing a microphysical model is to provide a physical description of the cloud vertical structure allowing for model simulation of CPR measurements and relating them to actual observations. For the purposes of this retrieval, the focus is placed on those key microphysical parameters to which the CPR holds sensitivity. Since clouds are composed of a distribution of particles (ice and/or water), of particular interest are physical parameters such as number concentration, geometrical dimension, mass, fall velocities, and rain rates. However, given the limited information that the CPR observing system offers, we are forced to focus our attention to only one of the above parameters. All others are to be parameterized in terms of this one particular parameter. Since the present work focuses on retrieving profiles of rain rates, this is the parameter of our choice. Moreover, even if clouds at some point in their evolution are in fact composed of a bimodal distribution of cloud particles and precipitating particles, the radar is mostly sensitive to the latter. Since a global parameterization that uniquely describes this bimodal repartition is not yet available, our choice is to represent clouds through a single particle distribution, tuned to describing precipitating particles. Obviously this approach would be valid only in precipitating clouds.

Following L'Ecuyer and Stephens (2002), we assume that all clouds can be described in terms of a Marshall–Palmer droplet size distribution (DSD):

$$n(D) = N_0 e^{-\Lambda D}, \quad (1)$$

where  $D$  is the diameter of the cloud particle. Using mass–diameter and fall velocity–diameter power laws (e.g., Liou 1992) that depend on a particle's shape and phase, one can relate the slope factor  $\Lambda$  to the rainfall rate  $\mathcal{R}$ :

$$\Lambda = a\mathcal{R}^b. \quad (2)$$

Although not universal, and only for the purpose of consistency with the work of Haynes et al. (2009), Table 1 shows the adopted values for these parameters. The adopted units for  $\mathcal{R}$  are millimeters per hour. In such a way we can retrieve our unknown variable of interest, the rainfall rate, from radar measurements (at each gate), through an inversion algorithm that is described in section 4. Since the rainfall rate is in fact related to the characteristic diameter of (1), then the cloud mass can also be evaluated. A quick sensitivity study of the above equation with respect to the above parameters sheds some light on the magnitude of error they may introduce. As such, the rain-rate relative error is  $1/b$  of the relative errors in parameter  $a$ , and respectively  $|\ln \mathcal{R}|$  of the relative errors in parameter  $b$ . For the cases we encounter, that translates into relative errors of  $\mathcal{R}$  less than about a factor of 7 of the relative errors of the above model parameters. Given the wide statistical nature of all of the above assumptions, the results that follow should only be interpreted from this point of view and not particularized for any given profile. This is still a work in progress that needs improvement to properly describe clouds at all scales of interest.

#### MIXED-PHASE PARAMETERIZATION

The microphysical model described above accounts for both ice crystals and water drops. Whereas ice crystals begin melting in regions where temperatures are above freezing, physics allows for the liquid phase to exist at temperatures as low as  $-40^\circ\text{C}$ . As such, profiles of temperature from numerical model runs are used to determine the cloud phase. Therefore, we allow for the possibility of mixed-phase clouds at temperature levels between  $-20^\circ$  and  $0^\circ\text{C}$  by imposing a precipitation mixture of ice (98%) and water (2%) between these two levels. To simulate the melting process, we gradually increase the water percentage to 100% within three gates following descent through the freezing level. For layers with temperatures below  $-20^\circ\text{C}$ , ice is the only phase allowed in the current algorithm.

#### b. 94-GHz reflectivity model

Described here is the radiative model (i.e., radar model) used to describe the scattering processes observed by *CloudSat*. We represent the radar equation in terms of modeled reflectivity  $Z_m$  as follows:

$$Z_m = Z + \text{MS} - \text{PIA}, \quad (3)$$

where  $Z$  is the total backscatter reflectivity (from clouds, or the surface), MS is the multiple-scattering contribution, and PIA is the path integrated attenuation that accounts for the two-way energy loss due to extinction

(scattering plus absorption) processes occurring between the radar and the range gate. Note that (3) is defined at all levels (or range gates). Obviously, of particular interest here are the range gates within the cloud and precipitation. However, we are interested in the return from the surface as well from the standpoint of its utility in deriving PIA—a column-integrated parameter that provides a natural constraint to the profiling algorithm (L'Ecuyer and Stephens 2002). This will be developed further below.

### 1) CLOUD PARTICLE RADAR MODEL

Under the assumption that the Mie regime is valid, the cloud particle radiative properties at 94 GHz, defined by (1) and (2), are computed as

$$X = \frac{\pi}{4} \int_0^{\infty} n(D) Q_X D^2 dD, \quad (4)$$

where  $X$  can be either the extinction, scattering, or backscatter coefficients, while  $Q_X$  is the corresponding Mie efficiency. The results are stored in the form of discretized lookup tables (LUT) for both snow and rain, as functions of temperature and rainfall rate. Future versions of the algorithm will have to account for various ice habits that can lead to significant departures from Mie theory. Since the above calculations are based on the distribution defined by (1), a sensitivity analysis similar to that performed above yields a factor on the order of  $1/6b$  between relative errors in  $\mathcal{R}$  and relative errors in  $N_0$ . We thus conclude that our retrieval model is relatively constrained with respect to the knowledge of forward model parameters.

### 2) PIA MODEL

PIA is significant at 94 GHz because of extinction processes in the entire atmospheric column (clear or cloudy):

$$\text{PIA}(H) = 20 \log(e) \int_0^H \sigma_{\text{ext}}(z) dz, \quad (5)$$

where  $\sigma_{\text{ext}}$  is the sum of extinction coefficients of all radiatively active atmospheric constituents and integration starts at the top of the atmosphere.

The principle gaseous atmospheric constituents that must be accounted for are water vapor ( $\text{H}_2\text{O}$ ),  $\text{O}_2$ ,  $\text{N}_2$ , and their impacts to attenuation as a function of temperature. Profiles of temperature and relative humidity from a numerical weather model are coupled with Liebe's (1989) work to provide extinction information. For cloudy atmospheres, the aforementioned LUT is used to determine the appropriate extinction coefficient given the rainfall rate and phase composition.

### c. MS effects

Multiply scattered photons are present in most remotely sensed signals. Since these events do not scale linearly with the scattering volume or its intrinsic single-scattering properties, their contribution to the total signal can vary dramatically. Although numerous past studies have grappled with this complicated problem (e.g., Miller and Stephens 1999; Mitrescu 2005), evaluations of MS contribution still lack in computational efficiency and overall accuracy because of the highly nonlinear nature of this problem. The MS problem is further complicated by the antenna gain pattern and any possible subgrid-scale inhomogeneity of the scattering volume.

Given the top view that CPR has, the MS builds up progressively as the signal penetrates deeper into the cloud, starting with the second-order term. Although higher-order terms may become dominant deeper into the cloud, that happens only in the cases of deep convective cloud systems, where we expect moderate-heavy precipitation events. Since the goal of the present work focuses on retrieving only light precipitation events (i.e., precipitation rates below  $5 \text{ mm h}^{-1}$ ), the multiple-scattering effects can be neglected from the definition of our forward model. However, as explained later on, MS effects are flagged through the definition of the cost function. Work is under way to implement a second-order scattering model that accounts for antenna pattern and is fast enough for semi-operational use.

### d. Surface $\sigma_0$ model

Inspection of (3), applied at surface levels, suggests the possibility of determining total column PIA from measurements of surface return. Although complicated by any MS effects, for a given surface type, the difference between surface measurements in a cloud-free atmosphere and a cloudy atmosphere is in fact total column PIA:

$$\text{PIA}_{\sigma} = \sigma_0 - \sigma, \quad (6)$$

where the subscript  $\sigma$  indicates the methodology for determining PIA. Here  $\sigma_0$  is the surface return in clear sky conditions corrected for atmospheric attenuation, while  $\sigma$  is the surface return for the particular cloudy scene also corrected for atmospheric attenuation. The basic assumption here is that the value for  $\sigma_0$  can be determined at all times, thus a universal constant for a given surface type. Then one can use (6), seen as a quasi-independent measurement, to constrain the computed (5) as will be shown later.

Using surface response under clear sky conditions (corrected for the atmospheric extinction), a  $\sigma_0$  database

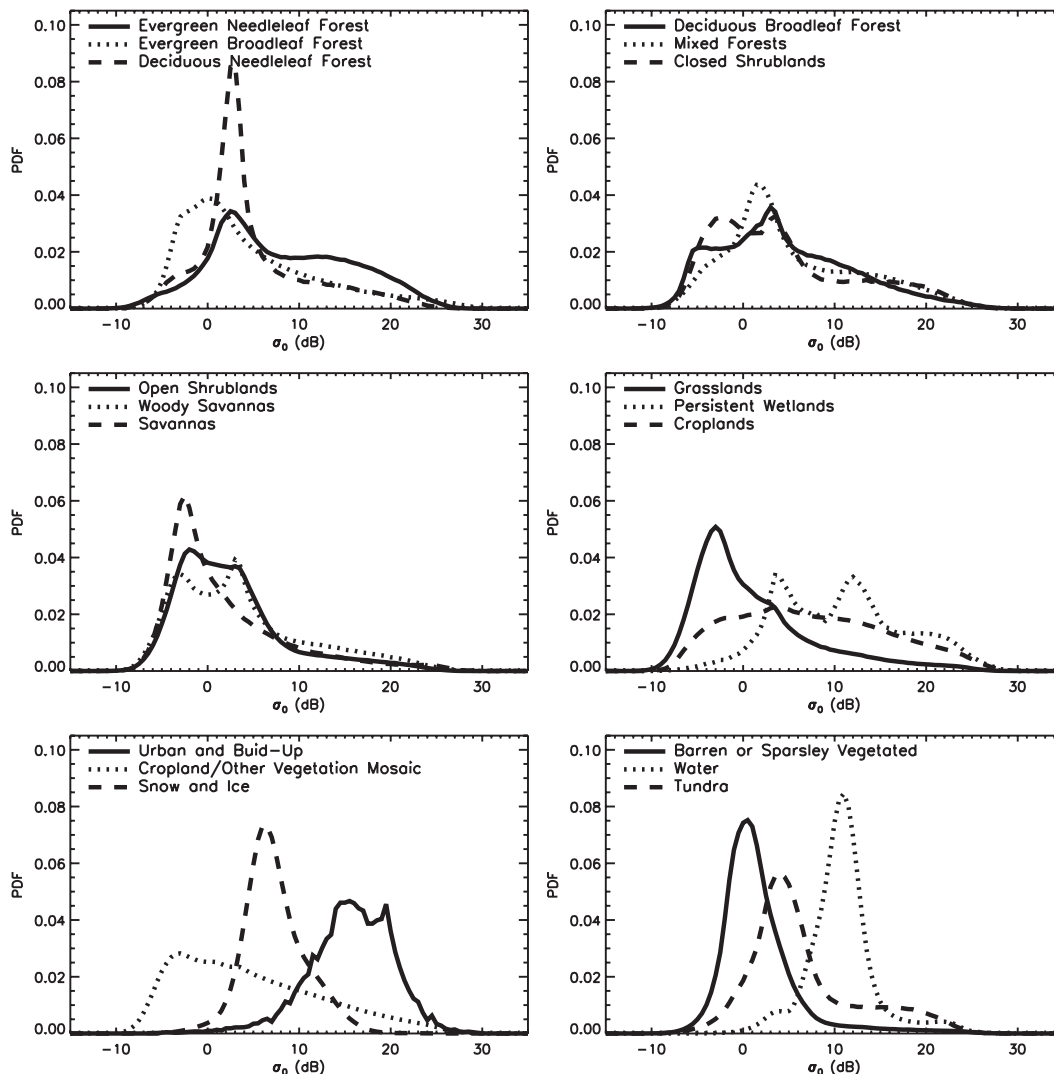


FIG. 1. PDF surface cross sections ( $\sigma_0$ ) for IGBP-classified surface types.

was constructed for the purpose of estimating  $PIA_{\sigma}$ . Since not all surfaces have the same radar response, the International Geosphere-Biosphere Programme (IGBP) surface type classification (Loveland et al. 2000) was used to stratify the data. Figure 1 shows the probability distribution functions (PDFs) for all surface types considered. The inferred mean values are used to compute  $PIA$  under cloudy conditions, using the measured  $\sigma_0$ , corrected for current atmospheric attenuation.

For water bodies, the histograms show a very tight relation confirming previous studies saying that this surface can be used for calibration purposes. As such, a reflectance model that depends on surface wind and sea surface temperature was developed (e.g., Cox and Munk 1954; Mitrescu et al. 2007; Haynes et al. 2009). For land surfaces, however, the spread is much higher because of a wider seasonal variation in canopy cover and

texture, but also because of terrain roughness and composition including moisture content. A model describing surface returns for these areas is much more complicated and is not essential for the scope of the present work.

#### e. Melting layer model

As ice crystals fall through the freezing layer, they start to melt. Because of a lack of a priori information (such as the ventilation factor), as introduced above, we assume that the melting process is linear with vertical depth. As such, a three-gate melting layer (i.e., for *CloudSat* this translates to 720 m) depth is assumed where both cloud drops and melting ice crystals are allowed. Below this level, all cloud particles are assumed to be water drops. Since we focus on light precipitation only, frozen precipitation from the deep convective system is not considered. Instead, these regions are simply

flagged as heavy precipitation and skipped. An additional problem is encountered for cases of temperature inversions. Here, we assume that the melting layer is the topmost freezing layer. The scattering properties of melted ice crystals are evaluated using the Maxwell–Garnett dielectric mixing formula as introduced by Menenghini and Liao (1996). We can thus write

$$\epsilon = \epsilon_i \frac{1 - 2fA}{1 + fA}, \quad \text{with} \quad A = \frac{\epsilon_i - \epsilon_w}{2\epsilon_i + \epsilon_w}, \quad (7)$$

where  $f$  is the fractional melted volume while  $\epsilon_i$  and  $\epsilon_w$  are the dielectric constants of ice and water, respectively. Lookup tables as functions of rainfall rate and melted fraction using (4) are generated. Although one could argue that smaller crystals melt faster than larger ones, the imposed melted fraction applies to the entire distribution. By gradually increasing the water content in this region, we in fact parameterize this process. As such, both the melted and water DSDs are invariant throughout the melting layer. Future versions of the algorithm should seek better parameterization for describing this complex process. We also want to point out that the above formulation is also being applied to the ice–air mixture (using a mass–diameter relationship for ice crystals).

#### 4. The inverse model

The retrieval (or inversion) method chosen for inferring profiles of precipitation rate is the optimal estimation technique. Described in detail in many papers (e.g., Jazwinsky 1970; L'Ecuyer and Stephens 2002; Rodgers 1976), it uses the forward model to minimize the cost function:

$$J = (\mathbf{R} - \mathbf{R}_a)^T \mathbf{S}_a^{-1} (\mathbf{R} - \mathbf{R}_a) + (\mathbf{Z}_o - \mathbf{Z}_m)^T \mathbf{S}_Z^{-1} (\mathbf{Z}_o - \mathbf{Z}_m) + (\text{PIA} - \text{PIA}_\sigma)^2 \mathbf{S}_\sigma^{-1}, \quad (8)$$

where  $\mathbf{Z}_o$  is the observed radar reflectivity,  $\mathbf{Z}_m$  is the modeled radar reflectivity,  $\mathbf{S}_a$  is the a priori error covariance matrix with its diagonal terms set to  $15 \text{ mm h}^{-1}$ , and  $\mathbf{S}_Z$  is the error covariance matrix associated with observations that has its diagonal terms set to  $2 \text{ dB}^2$ . We note that the  $\mathbf{S}_a$  formulation contains off-diagonal terms that account for model error cross correlation between various gates using an exponential decay function with a correlation length set to 2.5 km. The quantity  $\mathbf{R}_a$  is the a priori estimate of the precipitation rate while  $\mathbf{R}$  is the rain-rate profile to be retrieved. As mentioned above, additional information about modeled and observed PIA

due to hydrometeor attenuation is introduced via the last term of the cost function using a fixed covariance  $\mathbf{S}_\sigma$  that depends solely on the type of the surface (water or land). If for water bodies  $\text{PIA}_\sigma$  can be determined with relatively good accuracy (about 2 dB after wind and temperature correction), for land surfaces it displays large ambiguities (between 10 and 20 dB) that can create convergence problems. It also shows that over land the retrieval relies mostly on the measured profile. For this reason adequate error covariance matrices must be used. As such, one can control the information content to be used for the retrieval problem, by filtering out the less reliable information without completely ignoring it. As this is still a work in progress, fine tuning is still being pursued. The above formulation seeks the solution through successive iterations (i.e., a Gauss–Newton gradient method) and does not require the introduction of a separate inversion model since it only uses the forward model formulation. A clear advantage of such an approach resides in its simplicity, flexibility, and universality. Moreover, additional constraints can be easily added or removed from the above definition. The associated covariance matrix of the retrieved profile is also provided:

$$\mathbf{S}_R = [\mathbf{S}_a^{-1} + \mathbf{K}^T \mathbf{S}_Z^{-1} \mathbf{K} + (\text{PIA} - \text{PIA}_\sigma)^2 \mathbf{S}_\sigma^{-1}]^{-1}, \quad (9)$$

where  $\mathbf{K}$  is the kernel matrix or the weighting function representing the sensitivity of the radar model to the parameter being retrieved ( $\mathbf{R}$ ).

However, for complex problems, the optimal estimation may become computationally demanding, particularly for deep cloud structures, since it requires several matrix computations. In addition, for these systems, deep inside the cloud, the MS term becomes important. When neglected, the retrieved scattering properties at these gates are far larger than the expected values; this effect increases further below because of a higher attenuation correction. As such, the iterative method quickly becomes unstable as the cost function increases dramatically. Therefore, the value of the cost function is used to flag the MS effects, which are due to the presence of heavy precipitation, as shown below.

#### 5. Implementation

As explained above, *CloudSat's* CPR is sensitive to clouds and precipitation. Although not specifically separated in the proposed microphysical model, given the strong dependence of the reflectivity field on the size of the cloud particles, the precipitation regions yield higher reflectivity values because of increased particle sizes. Also, since the present algorithm seeks to evaluate cloud precipitation that falls to the ground, a series of tests and

thresholds are being employed to discriminate between precipitating and nonprecipitating clouds. The presence of ground clutter creates a real problem, especially for regions with low-level clouds over steep terrain. Temperature data from numerical model runs (produced operationally at the European Centre for Medium-Range Weather Forecasts) are also used to flag the precipitation phase. To keep consistency between the present profiling algorithm and that developed by Haynes et al. (2009), we adopt all the tests and thresholds defined within. More details about these two precipitation techniques can be downloaded from the Data Processing Center at Colorado State University (<http://CloudSat.cira.colostate.edu/dataSpecs.php>).

Given the size of the *CloudSat* files, and the probability of detecting any form of precipitation, one granule is being processed somewhere between 10 and 30 min on a 2.66-GHz dual-processor computer. Processing time increases more than 100 times when MS effects are considered, thus creating a serious limitation for near-real-time processing. Work is under way for testing and implementing fast multiple-scattering algorithms (e.g., Hogan 2008). Moreover, plans for adapting the attenuation technique used for inferring rainfall rates as introduced by Matrosov (2007) are being considered. That would ensure a larger range of retrieved rainfall rates using *CloudSat*'s 94-GHz CPR. In its present form, however, we limit ourselves to retrieving only light precipitation with rainfall rates less than about  $5 \text{ mm h}^{-1}$ . We also adopt the same rain likelihood flags as defined in the constant column precipitation algorithm (2C-PC) of Haynes et al. (2009). Despite this limitation, regions of higher-intensity precipitation are still being identified in the product but the algorithm does not provide quantitative rain-rate estimates because of the MS problem explained above.

## 6. Case study

This section summarizes results from the application of the retrieval technique to actual *CloudSat* data. To ensure quick validation to our results, we applied the above retrieval algorithm to an orbital segment that was collected when *CloudSat* was over the KLIX Next Generation Weather Radar (NEXRAD), near New Orleans, Louisiana, on 31 July 2006. Figure 2 (top panel) shows the radar profile as recorded by the CPR. Evident in the radar return is a nimbostratus cloud structure with echo tops around 12 km and with its base obscured by the rain signal. The bright band (BB), which can be clearly distinguished, is just below the freezing level as indicated by the temperature profile. Strong echoes near the surface suggest that precipitation was likely. The

figure also suggests some entrainment near cloud top and a change in the morphology of the cloud (i.e., a two-layer cloud structure emerges) as the scan progresses north. Figure 2 (second panel) demonstrates the profiling capabilities of *CloudSat* and both the performances and limitations of the present retrieval algorithm as it shows profiles of the retrieved LWC and ice water content (IWC) only for cases where the precipitation flag is set. Because of the ground clutter problems, only gates above 1 km are being processed. The melting layer is again clearly visible with retrieved values of up to  $500 \text{ mg m}^{-3}$ . For demonstration purposes, Fig. 2 (third panel) shows the unattenuated 94-GHz reflectivity field corresponding to the above distribution of hydrometeors. This is nothing more than the application of the forward model to the retrieved LWC and IWC profiles. Moreover, the reflectivity field just below the bright band appears quasi-uniform, a basic assumption employed by the other two *CloudSat* precipitation models as mentioned below. Moreover, the MS effects, neglected here, become important for lower layers as the reflectivity field shows values exceeding the 15-dBZ threshold. However, because of the additional constrain given by PIA, the retrieved rain rates are not far from those inferred using other techniques and/or data. Figure 2 (bottom panel) shows the rain rates inferred using *CloudSat* data applied to three different algorithms and one using KLIX radar data (extracted along *CloudSat* track). The latter is converted into rainfall rates using the default ( $Z-R$ ) relationship for the Weather Surveillance Radar-1988 Doppler (WSR-88D) radar network written as  $R = 0.017Z^{0.714}$  and shown with the green line. The black line denotes results using the present algorithm. As an additional comparison, the blue line represents the approach described by Matrosov (2007), where an extinction versus rain-rate ( $k-R$ ) relationship is being employed. However, since this approach works only in regions below the bright band, a gap in this data field is noted. The red line shows the rain rates equivalent to a uniform cloud layer as described by Haynes et al. (2009), where only PIA information is used to infer a rain rate. Since this approach is only applicable over ocean surfaces, the comparison can only be performed for the first half of the data points (i.e., over ocean). Finally, the along-*CloudSat* track rain rates as retrieved using the AMSR-E passive microwave (PMW) sensor onboard *Aqua* are presented with an orange line. For this particular case, overall, the agreement between all these various retrieval schemes (and/or sensors) is satisfactory. However, we note pronounced spikes in the retrieval around 1919:44 UTC. Here the BB signature is obviously close to or below the measurement error and the only option is the use of the NWP temperature profile for its placement. Therefore, in the absence of

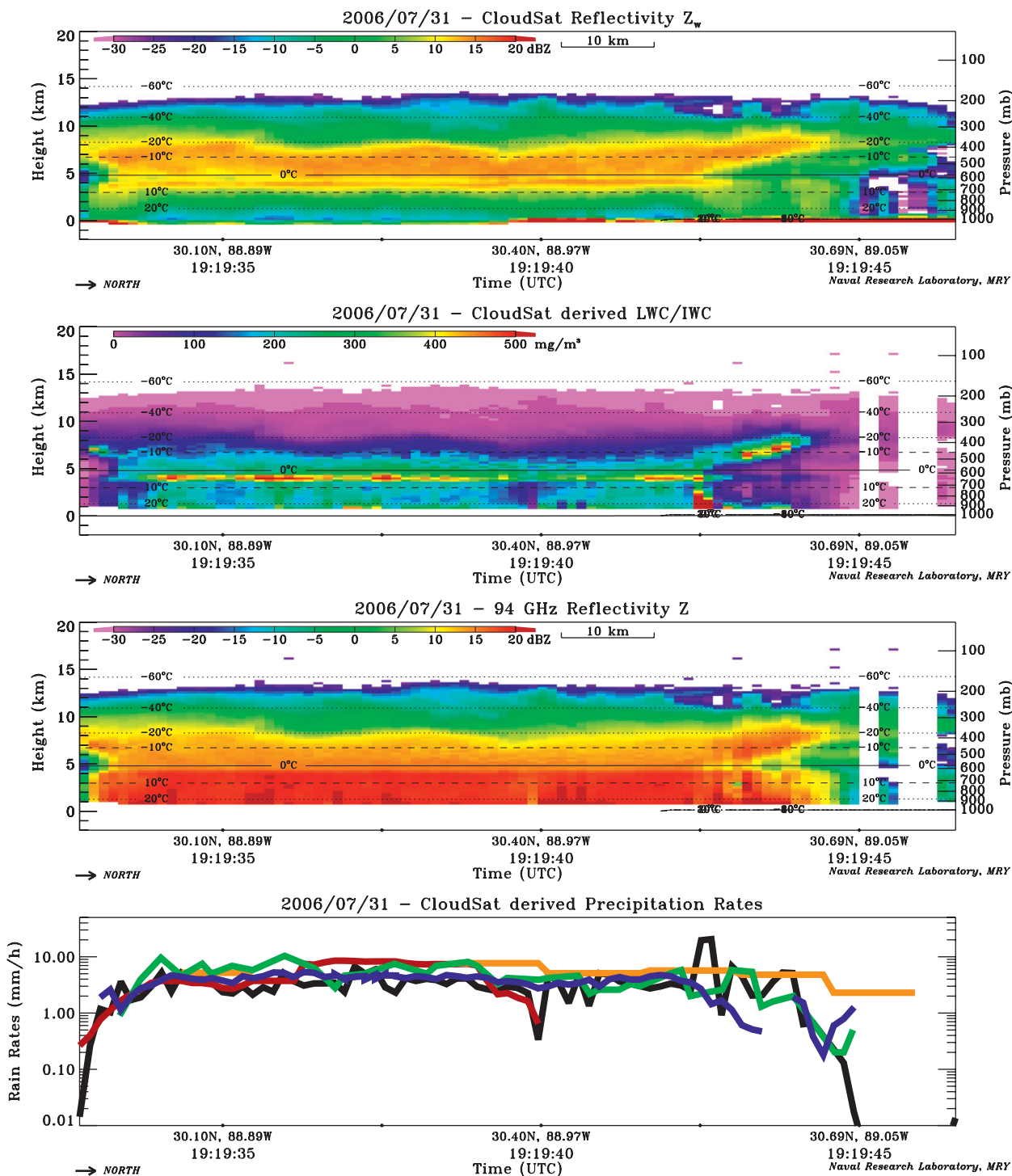


FIG. 2. Case study of 31 Jul 2006 near KLIX NEXRAD radar. (top) *CloudSat* reflectivity, (second from top) retrieved profiles of LWC and IWC, (third from top) simulated 94-GHz reflectivities using retrieved LWC and IWC profiles, and (bottom) rainfall rates using (i) present method (black line), (ii) *k-R* method (Matrosov 2007; blue line), (iii) PIA-based method (Haynes et al. 2009; red line), (iv) KLIX *Z-R* relationship (green line), and (v) AMSR-E-derived precipitation rates (orange line).

a detectable BB, the forward model is thus slightly incorrect in its BB formulation (i.e., placement and extent, but also in describing the mixed phase). These artifacts are amplified by the ground clutter effect and the neglect of the MS term. Similar retrieval behavior, but less pronounced, is seen in KLIX data. Also apparent is the effect of the CPR footprint on the superior resolution of the ground radars.

## 7. Statistical results

To further test the algorithm output, we run it for the entire year of 2007. As explained above, since the MS effects are neglected, the retrieval will not converge for regions where rainfall rate is above or around  $5 \text{ mm h}^{-1}$ . These regions are flagged by the large values in the cost function (8). Although no retrieved values are reported in these cases, they are flagged as heavy precipitation regions. As such, we can distinguish three regions of interest: clear, light precipitation, and heavy precipitation. The retrieval runs on a global domain, regardless of the underlying surface, or the presence of a melting layer, or precipitation type that can somehow be seen as a limiting factor. However, as mentioned above, even if the aim of the paper is to introduce the grounds for a precipitation profiling algorithm, given the limitations of both the observing system as well as the crudeness of the forward model, the results should be interpreted with care.

As mentioned in the previous section, two other precipitation algorithm datasets are available: the 2C-PC and the AMSR-E PMW precipitation product. Keeping in mind that none of these three algorithms represents the ground truth, the following discussion only contrasts their output. Since precipitation is characterized by both intensity and incidence, we decided to present this comparison study as divided into three main intensity-based categories: (i) very light precipitation with rain rates less than  $1 \text{ mm h}^{-1}$ ; (ii) light–moderate precipitation with rain rates between  $1$  and  $5 \text{ mm h}^{-1}$ ; and (iii) heavy precipitation with rain rates more than  $5 \text{ mm h}^{-1}$ . The probability of rainfall in each of these categories as inferred by all three algorithms is presented in Figs. 3, 4, and 5, where each of the three panels (from top to bottom) shows, in order, outputs from the present, 2C-PC, and AMSR-E PMW algorithms, respectively. Despite possible problems due to differences in ground resolution, for consistency purposes, only AMSR-E pixels closest to the *CloudSat* footprint were considered. Given the sampling geometry that CPR has combined with the A-Train orbital pass characteristics, the results capture only a global 0130–1330 local time snapshot of the precipitation field. Overall, similar precipitation patterns and

regions can be observed in all three intensity-based categories, although the frequency of occurrence can vary dramatically from one category to another and/or one algorithm to another. Associated with either short-lived convective regions or more persistent frontal regions, light precipitating clouds are a common feature within the general weather pattern features. Clearly discernible are the Southern Hemisphere (SH) storm tracks—a manifestation of the zonality in circulation—which produce considerable amounts of very light precipitation, mostly due to frontal activity. Not as clearly defined are the precipitating events associated with the Northern Hemisphere (NH) storm tracks, influenced by the larger distribution of land surfaces. As with the SH, a wave structure due to frontal passages is visible. The intertropical convergence zone (ITCZ) around the equator is also well captured despite the decrease in spatial coverage due to the polar orbit placement. Also captured is the South Pacific convergence zone (SPCZ) as well as the precipitation due to the monsoon cycle in the Arabian Sea and Bay of Bengal. Over land, we note the both convective and orographically induced precipitation features over elevated regions in South America, Africa, and Tibet due to the higher frequency and/or longer lifetime that such cloud systems have. On the opposite side, low (or nonexistent) precipitation regions like subtropical belts, Australia, the Arabic Peninsula, or the Sahara are also being resolved by this analysis. However, because of the ground clutter problem, well known low marine stratus regions, like those near California, Chile, West Africa, etc., that have the potential of producing light precipitation are misdiagnosed by the CPR. Since that happens to all the low clouds over the entire globe, caution is required when interpreting these results.

Figure 3 shows the incidence of very light precipitation. Somehow expected, the present algorithm (top panel) contrasts the most with the other two methods. It clearly identifies the SH and NH storm tracks as the most persistent precipitation regions, with probability rates that exceed 20%. In this case, we show all possible very light precipitating events (i.e., retrieved reflectivities at the lowest bin with values greater than  $-15 \text{ dBZ}$ ). Although very light (with average rain rates less than  $0.5 \text{ mm h}^{-1}$ ), these regions may exert an important influence on the global heating rates and the nonlinear cloud–climate interactions. Very light precipitation events over ocean bodies clearly exceed those over land surfaces. These findings are in sharp contrast to the other two methods. The 2C-PC method (middle panel), tuned only to liquid precipitation, shows a decrease in precipitation events as we move poleward, due to an increase in solid precipitation events. As expected, the AMSR-E PMW-based algorithm (bottom panel) fails to reveal most of the very

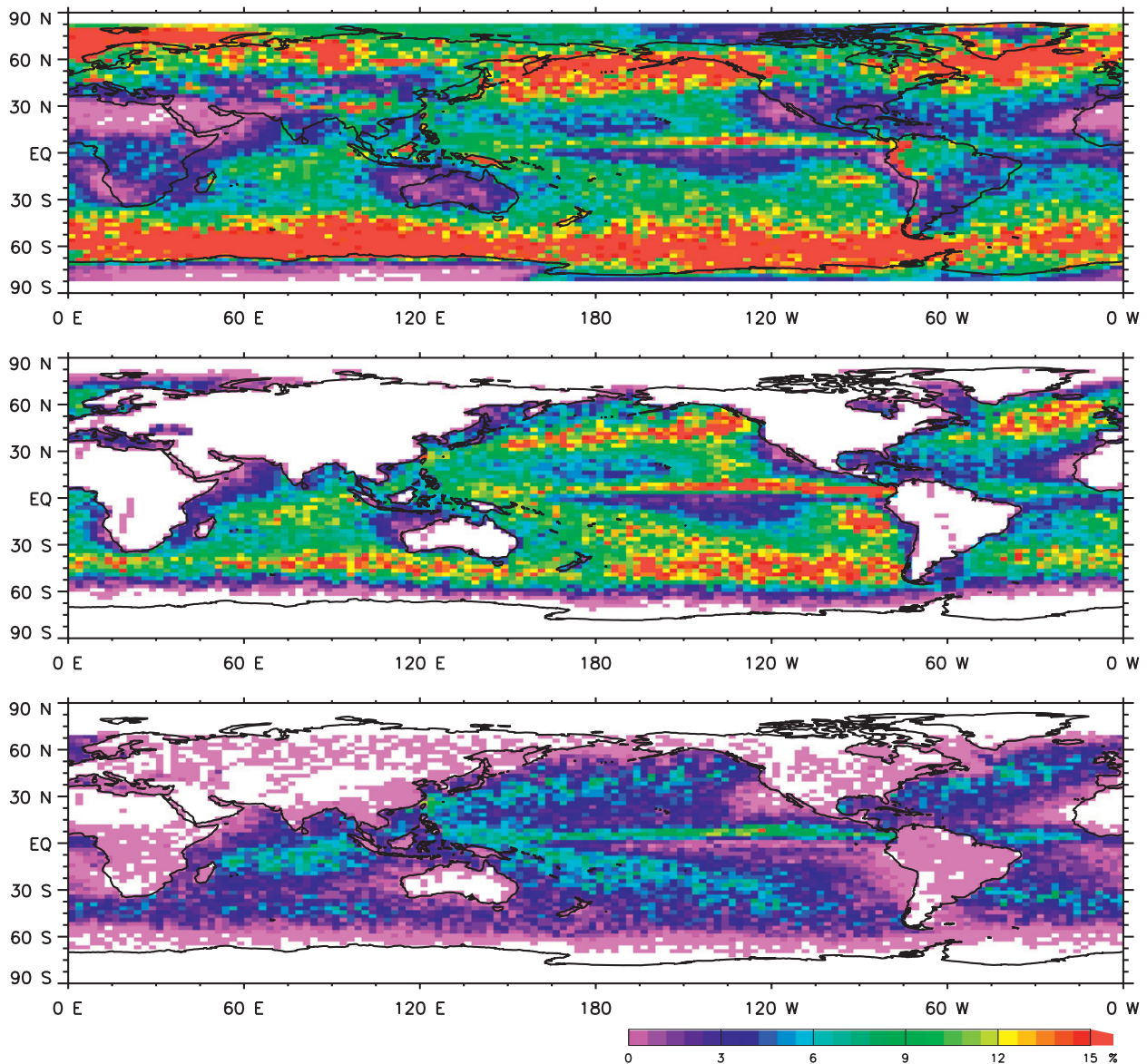


FIG. 3. Very light precipitation events (2007). (top) Present work, (middle) 2C-PC algorithm, and (bottom) AMSR-E PMW algorithm.

light precipitation regions, especially those occurring at higher latitudes.

Figure 4 shows the precipitation event frequencies for light–moderate precipitation rates. Here all three algorithms produce more or less the same global patterns as identified before, but quantitative differences are still evident. If 2C-PC indicates frequencies of up to 5% (middle panel), the current algorithm shows only a factor of about 3% (top panel), while the PMW lies somewhere in between these values (bottom panel). Again, we note the sharp contrast between ocean and land precipitation events at the time of the sampling.

Figure 5 shows the event distribution of heavy precipitation. On average, all three methods identify the same

regions: ITCZ, SPCZ, Indian Ocean, and convective regions over Africa and South America (not reported by the 2C-PC algorithm since over land). Although the heavy precipitation events are well correlated with very light and light–moderate precipitation events, we note that regions like equatorial South America, Africa, and Indonesia are more prone to this type of precipitation. Again we note that the PMW algorithm (bottom panel) does not identify any heavy precipitation events in either the NH or SH storm-track regions; however, for all other regions the level of agreement between all three algorithms is best for this precipitation category. Although the land–ocean precipitation event contrast is still visible, heavy precipitation event frequencies over

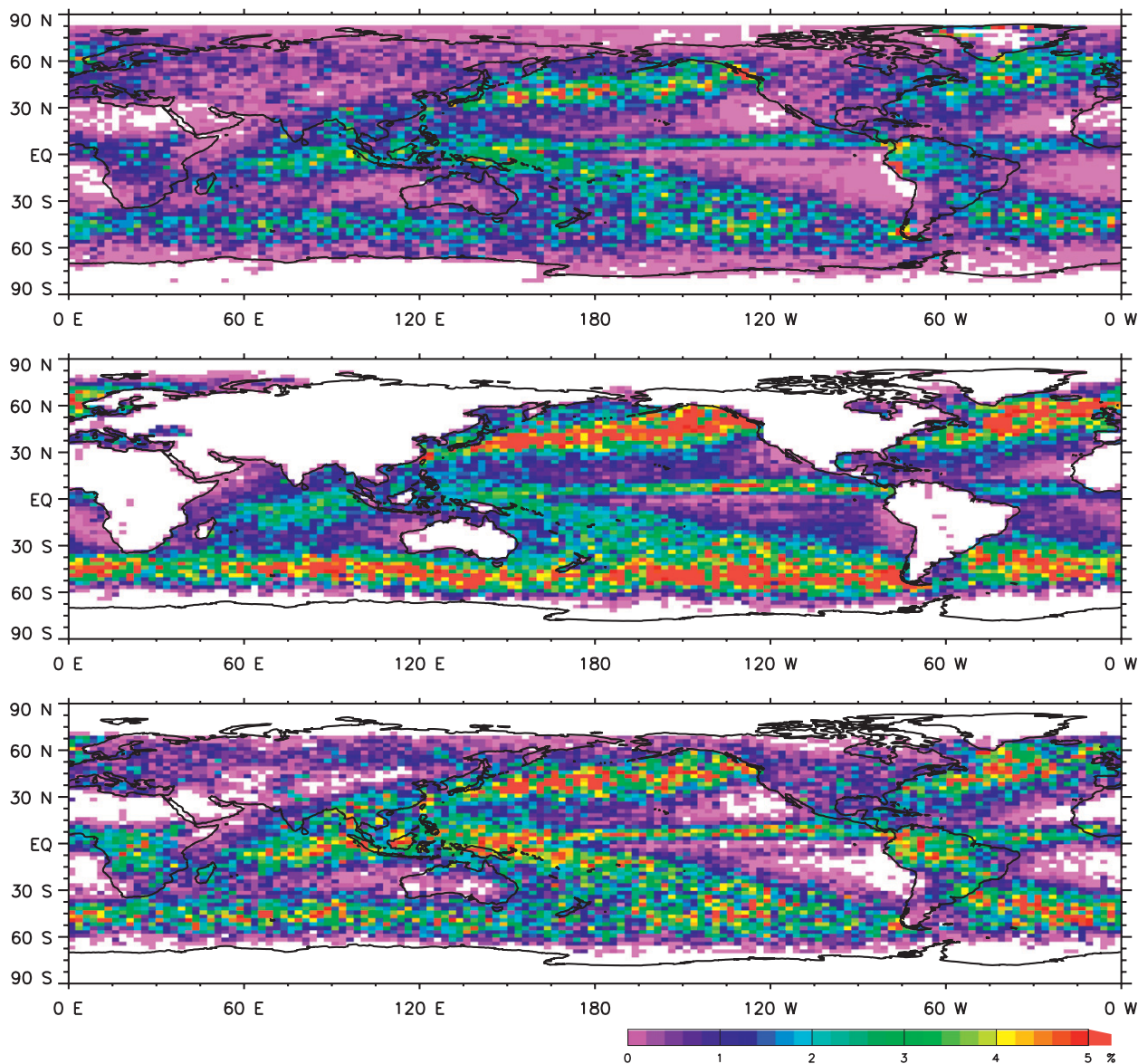


FIG. 4. As in Fig. 3, but for light-moderate precipitation.

some land regions can be as high as those over ocean regions.

Although still a work in progress, the present *CloudSat* algorithm shows very close similarities with the global distribution of precipitation events and intensities as reported by the Comprehensive Ocean-Atmosphere Data Set (COADS), which extracts its information using global ship weather reports (Petty 1995, 1997). Since precipitation is cloud dependent, all of these statistics also shed some light onto other cloud-related effects, such as radiative and dynamic effects, thus the importance of such studies.

## 8. Conclusions

The present work explores the feasibility of using 94-GHz spaceborne radar data for detecting and quantifying light-moderate rainfall rates. Examination of the *CloudSat* data reveals promising results that lend hope to the notion that a very important component of the earth's hydrological cycle can at last be measured on the global scale.

Future work must expand the use of a modeled surface return to land surfaces (as applied to the IGBP histograms), while improving the current model of water

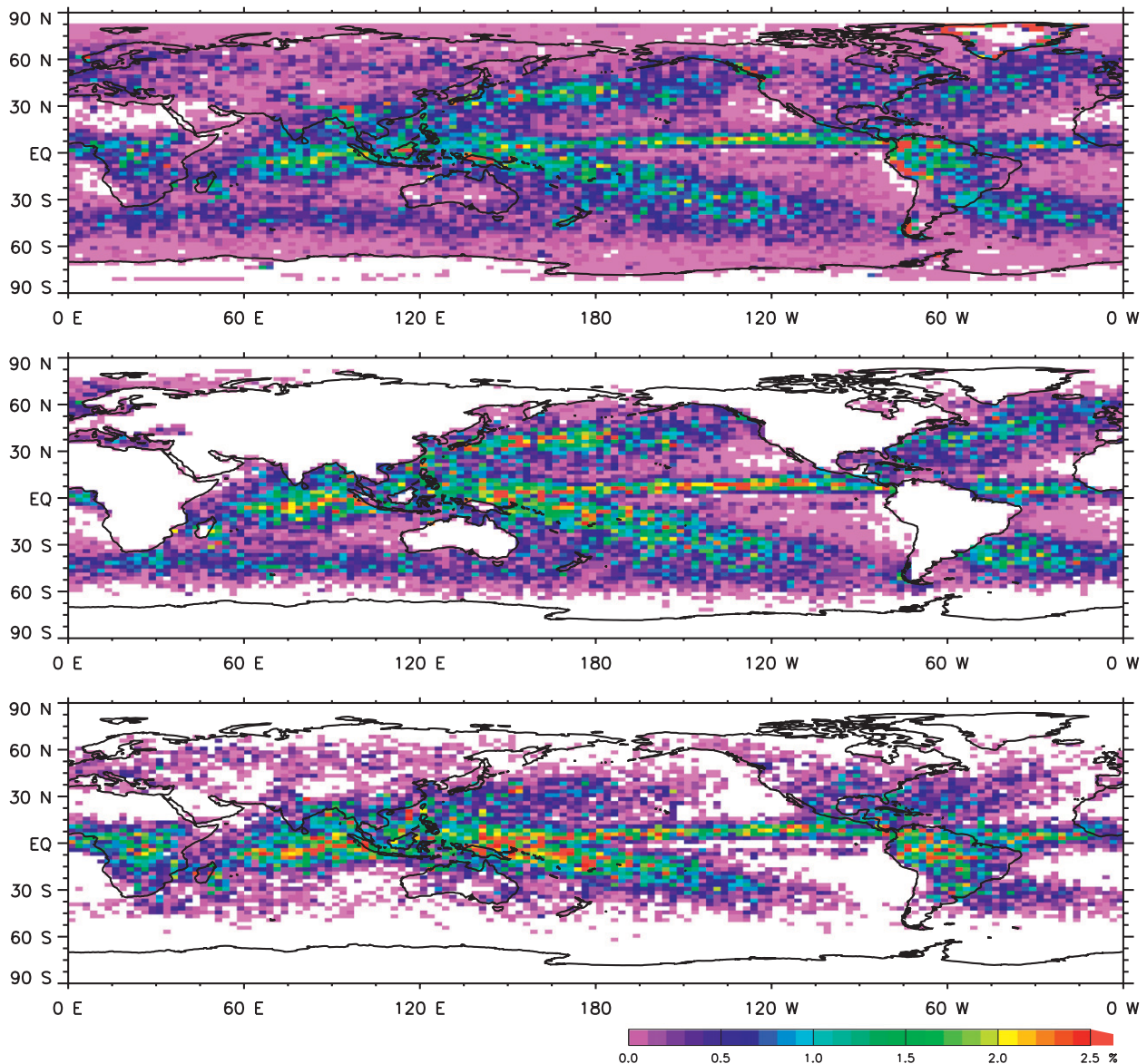


FIG. 5. As in Fig. 3, but for heavy precipitation.

surface reflectivity return. Also, resulting in part from the large size of the sampled volume by the CPR sensor compared to the ground radars, the effect of multiply-scattered radiation must be taken into account (particularly in moderate rain regimes), either in terms of a filter or an account made in the forward model based, for example, on Monte Carlo simulations. The MS effect is most pronounced at the farthest range gates where surface rain rates are being evaluated, and increases dramatically with the amount of cloud-rainwater mass residing in the column above. Moreover, an improved algorithm for brightband detection and a more realistic mixed-phase description are being tested for the next versions of the *CloudSat* precipitation profiling algorithm.

Our ultimate goal is to produce a global quantitative analysis of light precipitation for the entire *CloudSat* mission. Since *CloudSat* is in a sun-synchronous orbit (1330 local time, ascending node), it should be acknowledged that precipitation estimates are biased by nonuniform diurnal sampling. Moreover, because of the ground clutter that is present in the *CloudSat* signal we are compelled at this early stage in data processing to consider only radar returns from gates that are approximately 1.25 km and higher above the surface for characterizing surface rainfall. Thus, shallow, low-level clouds (predominantly marine stratocumulus systems) were excluded from these precipitation statistics. However, a new clutter filter approach should partially alleviate

this problem and help push this limit somewhere close to the 720-m range. Despite these shortcomings, these preliminary findings are encouraging as they correlate well with the other *CloudSat* precipitation algorithm (2C-PC), AMSRE-E PMW algorithm, and/or ship observations (COADS). These positive results not only add quantitative information to the general knowledge of clouds and precipitation, but also help to place *CloudSat* in the context of better-known precipitation sensors.

*Acknowledgments.* The support of our sponsors, NASA Earth Science Division Radiation Sciences Program *CloudSat* light precipitation project (NNG07H43i), and the Office of Naval Research under Program Element PE-0602435N, is gratefully acknowledged.

#### REFERENCES

- Cox, C., and W. Munk, 1954: Measurements of the roughness of the sea surface from photographs of the sun's glitter. *J. Opt. Soc. Amer.*, **144**, 838–850.
- Haynes, J. M., T. S. L'Ecuyer, G. L. Stephens, S. D. Miller, C. Mitrescu, N. B. Wood, and S. Tanelli, 2009: Rainfall retrieval over the ocean with spaceborne W-band radar. *J. Geophys. Res.*, **114**, D00A22, doi:10.1029/2008JD009973.
- Held, I. M., and B. J. Soden, 2000: Water vapor feedback and global warming. *Annu. Rev. Energy Environ.*, **25**, 441–475.
- Hogan, R., 2008: Fast lidars and radar multiple-scattering models. Part I: Small-angle scattering photon using the photon variance-covariance method. *J. Atmos. Sci.*, **65**, 3621–3635.
- Jazwinsky, A. H., 1970: *Stochastic Processes and Filtering Theory*. Academic Press, 376 pp.
- Lebsock, M. D., G. L. Stephens, and C. Kummerow, 2008: Multi-sensor satellite observations of aerosol effects on warm clouds. *J. Geophys. Res.*, **113**, D15205, doi:10.1029/2008JD009876.
- L'Ecuyer, T., and G. L. Stephens, 2002: An estimation-based precipitation retrieval algorithm for attenuating radars. *J. Appl. Meteor.*, **41**, 272–285.
- Liebe, H., 1989: MPM89—An atmospheric mm-wave propagation model. *Int. J. Infrared Millimeter Waves*, **10** (6), 631–650.
- Liou, K. N., 1992: *Radiation and Cloud Processes in the Atmosphere*. Oxford University Press, 487 pp.
- Loveland, T. R., B. C. Reed, J. F. Brown, D. O. Ohlen, Z. Zhu, L. Yang, and J. W. Merchant, 2000: Development of a global land cover characteristics database and IGBP DISCover from 1 km AVHRR data. *Int. J. Remote Sens.*, **21** (6–7), 1303–1330.
- Mace, G. G., Q. Zhang, M. Vaughan, R. Marchand, G. Stephens, C. Trepte, and D. Winker, 2009: A description of hydrometeor layer occurrence statistics derived from the first year of merged *CloudSat* and CALIPSO data. *J. Geophys. Res.*, **114**, D00A26, doi:10.1029/2007JD009755.
- Matrosov, S. Y., 2007: Potential for attenuation-based estimations of rainfall rate from *CloudSat*. *Geophys. Res. Lett.*, **34**, L05817, doi:10.1029/2006GL029161.
- Menenghini, R., and L. Liao, 1996: Comparisons of cross sections for melting hydrometeors as derived from dielectric mixing formulas and a numerical method. *J. Appl. Meteor.*, **35**, 1658–1670.
- Miller, S. D., and G. L. Stephens, 1999: Multiple scattering effects in the lidar pulse stretching problem. *J. Geophys. Res.*, **104** (D18), 22 205–22 220.
- Mitrescu, C., 2005: Lidar model with parameterized multiple scattering for retrieving cloud optical properties. *J. Quant. Spectrosc. Radiat. Transfer*, **94**, 210–224.
- , J. M. Haynes, T. L'Ecuyer, S. D. Miller, and J. Turk, 2007: Light rain retrievals using *CloudSat* 94-GHz radar data—Preliminary results. Preprints, *14th Symp. on Meteorological Observation and Instrumentation and 16th Conf. on Applied Climatology*, San Antonio, TX, Amer. Meteor. Soc., JP2.6. [Available online at <http://ams.confex.com/ams/pdfpapers/117883.pdf>.]
- , S. D. Miller, J. Hawkins, T. L'Ecuyer, J. Turk, P. Partain, and G. L. Stephens, 2008: Near-real-time applications of *CloudSat* data. *J. Appl. Meteor. Climatol.*, **47**, 1982–1994.
- Petty, G. W., 1995: Frequencies and characteristics of global oceanic precipitation from shipboard present-weather reports. *Bull. Amer. Meteor. Soc.*, **76**, 1593–1616.
- , 1997: An intercomparison of oceanic precipitation frequencies from 10 special sensors microwave/imager rain rate algorithms and shipboard present weather reports. *J. Geophys. Res.*, **102**, 1757–1777.
- Rodgers, C., 1976: Retrievals of atmospheric temperature and composition from remote measurements of thermal radiation. *Rev. Geophys. Space Phys.*, **14**, 609–624.
- Stephens, G. L., and Coauthors, 2002: The *CloudSat* mission and the A-Train: A new dimension of space-based observations of clouds and precipitation. *Bull. Amer. Meteor. Soc.*, **83**, 1771–1790.